Journal of
MATERIALS RESEARCH

Overview
DOI:10.1557/s43578-021-00458-1

ULTRA-WIDE BANDGAP MATERIALS, DEVICES, AND SYSTEMS

FOCUS ISSUE

Ultrawide-bandgap semiconductors: An overview

Man Hoi Wong[1,a), Oliver Bierwagen[2], Robert J. Kaplar[3], Hitoshi Umezawa[4]
[1] *Department of Electrical and Computer Engineering, University of Massachusetts Lowell, Lowell, MA 01854, USA*
[2] *Paul-Drude-Institut für Festkörperelektronik, Leibniz-Institut im Forschungsverbund Berlin e.V., Hausvogteiplatz 5–7, 10117 Berlin, Germany*
[3] *Sandia National Laboratories, Albuquerque, NM 87123, USA*
[4] *Advanced Power Electronics Research Center, National Institute of Advanced Industrial Science and Technology, Osaka 563-8577, Japan*
[a)] Address all correspondence to this author. e-mail: manhoi_wong@uml.edu

Received: 23 November 2021; accepted: 3 December 2021; published online: 28 December 2021

Ultrawide-bandgap (UWBG) semiconductor technology is presently going through a renaissance exemplified by advances in material-level understanding, extensions of known concepts to new materials, novel device concepts, and new applications. This focus issue presents a timely selection of papers spanning the current state of the art in UWBG materials and applications, including both experimental results and theoretical developments. It covers broad research subtopics on UWBG bulk crystals and substrate technologies, UWBG defect science and doping, UWBG epitaxy, UWBG electronic and optoelectronic properties, and UWBG power devices and emitters. In this overview article, we consolidate the fundamentals and background of key UWBG semiconductors including aluminum gallium nitride alloys ($Al_xGa_{1-x}N$), boron nitride (BN), diamond, β-phase gallium oxide (β-Ga_2O_3), and a number of other UWBG binary and ternary oxides.

Ultrawide-bandgap (UWBG) semiconductors, with bandgap energies much greater than the 3.4 eV of GaN or 3.2 eV of SiC, represent an emerging new area of intensive research covering a wide spectrum of materials, physics, devices, and applications [1]. As the critical electric field of avalanche breakdown increases super-linearly with increasing bandgap energy (detailed analysis discussed in a recent study led by Sandia and MIT Lincoln Lab [2]), UWBG semiconductors can tolerate high fields to enable high-power electronic devices for telecommunications, motor drives, power grid, electric vehicles, industrial and locomotive traction control, and various other applications. In addition, light emission from UWBG materials occurs in the deep ultraviolet (UV) part of the electromagnetic spectrum, which is attractive for extending the working wavelengths of photonic devices beyond the UV–visible (UV–vis) spectrum to enable potential applications in deep-UV optoelectronics, quantum information science, and bio-chemical sensing. This new class of semiconductors is also being explored for device applications in harsh environments by taking advantage of their thermal stability and radiation hardness. Compared to the development of GaN and SiC, all UWBG materials are relatively immature and still at a nascent stage. Most research efforts in UWBG focus on aluminum gallium nitride alloys ($Al_xGa_{1-x}N$), boron nitride (BN), diamond, and a large family of binary (typified by β-phase gallium oxide (β-Ga_2O_3)) and ternary oxide semiconductors. The extensive research activities on these materials are motivated by their reliable dopability and high carrier mobilities, the availability of substrates for thin-film growth, and successful demonstrations of devices. In this article, we provide an overview of the aforementioned different types of UWBG semiconductors, whose recent developments and state of the art in materials and applications are featured in this focus issue.

AlGaN

$Al_xGa_{1-x}N$ is an alloyed UWBG semiconductor that typically possesses a hexagonal wurtzite structure. Its bandgap can be tuned from 3.4 eV (GaN at $x = 0$) to over 6 eV (AlN at $x = 1$) by varying the aluminum composition x in the material [1]. This tunability permits the ready formation of heterostructures [3], which allows great flexibility in the types of electronic devices that can be realized. Additionally, because it is a direct-gap semiconductor, it is suitable for the fabrication of UV emitters. Visible- and solar-blind photodetectors have also been demonstrated [4]. $Al_xGa_{1-x}N$ can be doped n-type by incorporating Si, which is a shallow impurity up to a composition x of 80–85% [5]. Mg is used as a p-type dopant, although it is somewhat deep in the gap for GaN (~ 160 meV) and becomes deeper as the Al composition x is increased [6]. In addition to impurity doping, a great advantage of $Al_xGa_{1-x}N$ is the presence of spontaneous and piezoelectric polarization [7], which aids in doping of the material through the formation of two-dimensional electron gases (2DEGs) as well as three-dimensional electron slabs [8]. Additionally, this approach of polarization-induced doping overcomes the large thermal activation energy of Mg and enables efficient p-type doping by field-ionizing the acceptors [9]. Growth of $Al_xGa_{1-x}N$ is typically done by metal–organic chemical vapor deposition (MOCVD), but other growth techniques have also been employed, such as plasma-assisted molecular beam epitaxy (MBE) [10]. $Al_xGa_{1-x}N$ may also be grown on a variety of substrates including sapphire, although growth on AlN substrates is becoming more common and has been instrumental for electronic devices [11] as well as UV optoelectronics. Growth on GaN [12] and even Si [13] substrates is also possible. While $Al_xGa_{1-x}N$ is typically grown in the polar c-orientation, growth of semi-polar $Al_xGa_{1-x}N$ has also been reported [14]. The physics of deep levels in $Al_xGa_{1-x}N$ is likewise a very rich topic, with sensitivity to growth conditions and Al composition documented [15]. Deep levels are critical not only because they can compensate intentional impurity dopants [16], but also because they can impact electronic device performance due to carrier trapping and de-trapping and optical device performance due to absorption and non-radiative recombination. $Al_xGa_{1-x}N$ may also potentially be used in photonic integrated circuits with applications in positioning, navigation, and timing [17].

Numerous electronic and optoelectronic devices have been demonstrated by groups around the world. The breakdown electric field is expected to increase approximately quadratically with the $Al_xGa_{1-x}N$ bandgap [18], and this has enabled power switching devices based both on lateral-transport $Al_xGa_{1-x}N/Al_yGa_{1-y}N$ heterostructures [19] and on vertical-transport devices with thick drift layers such as pn diodes [20] and Schottky diodes [21]. Moreover, the high breakdown electric field coupled with the favorable carrier velocity saturation properties of $Al_xGa_{1-x}N$ [22] has permitted the demonstration of radio-frequency devices with encouraging performance [23]. One challenge with electronic devices is alloy scattering, which impacts not only the low-field mobility [24] but also the thermal conductivity. An additional major challenge is the formation of ohmic contacts, and various approaches not only to achieve linear contacts but also to reduce the specific contact resistivity have been demonstrated, including compositional grading [25]. Similarly, the integration of dielectrics on $Al_xGa_{1-x}N$ is a topic of current research, which is especially challenging due to the large bandgap of the semiconductor and the resulting small conduction-band offset with the dielectric [26]. Regarding optoelectronics, the ultrawide direct bandgap of $Al_xGa_{1-x}N$ has permitted the realization of UV emitters including light-emitting diodes [27] and lasers [28], with applications such as water purification in mind, and such devices are now commercially available. Several representative figures from a review paper on $Al_xGa_{1-x}N$-based UV optoelectronics by Kirste et al. [29] are reproduced below and are intended to convey key aspects of $Al_xGa_{1-x}N$, notably the high quality of epitaxy in Fig. 1 and exemplary device performance in Fig. 2.

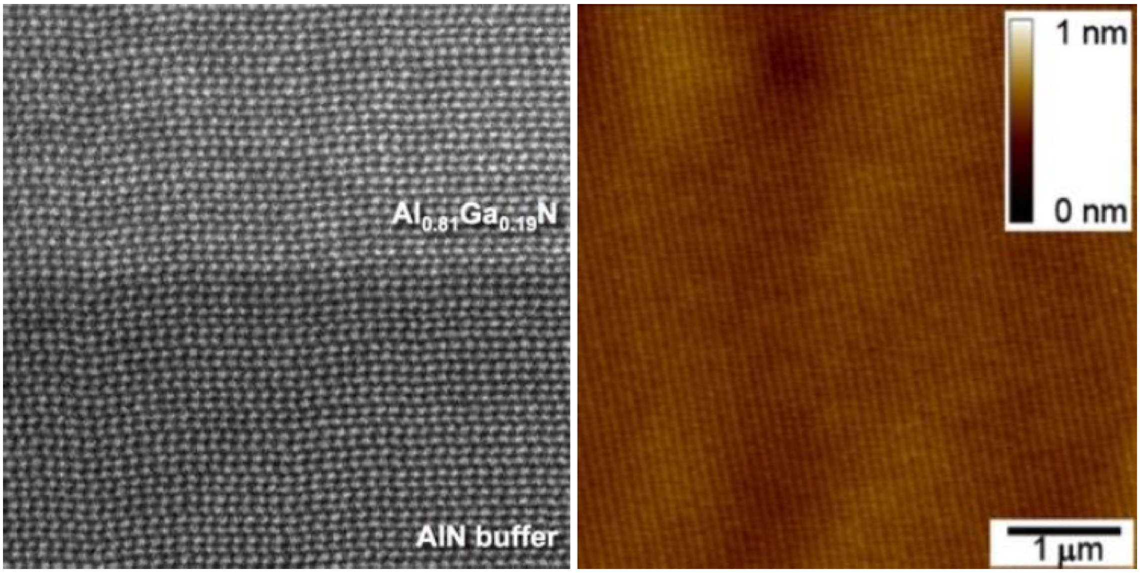

Figure 1: (Left) High-resolution transmission electron microscopy image of $Al_{0.8}Ga_{0.2}N$ grown on AlN. (Right) 5 × 5 µm² atomic force microscopy image of $Al_{0.7}Ga_{0.3}N$ grown on AlN with root-mean-square roughness of less than 50 pm. Reprinted by permission from [29], copyright 2021.

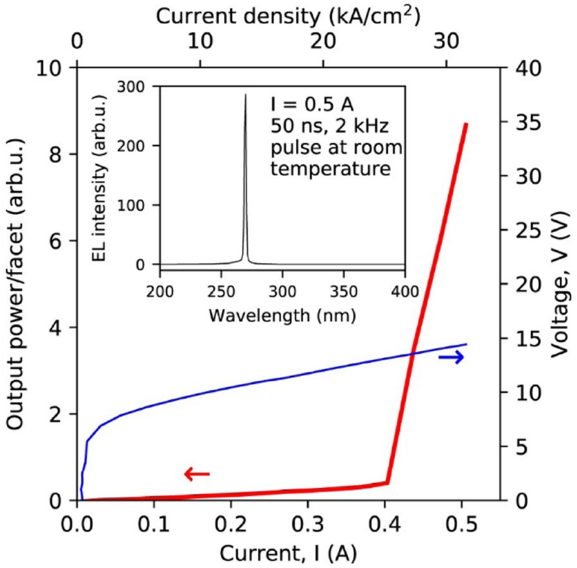

Figure 2: (Main Figure) Voltage (blue curve) and optical output power (red curve) plotted vs. absolute current (bottom axis) and current density (top axis) for $Al_xGa_{1-x}N$-based UV edge-emitting diode. (Inset) Electroluminescence spectrum showing emission at around 271 nm. Reproduced, with permission, from [28]. Copyright (2019), the Japan Society of Applied Physics.

BN

BN is a compound isoelectronic with carbon. Like carbon, BN can possess sp^2- and sp^3-bonded phases [30], which are the analogs of graphite and diamond, respectively. The thermodynamically stable phase under standard temperature and pressure is sp^2-bonded hexagonal BN (h-BN), whose wide bandgap of ~ 6 eV and ability to form single layers make it especially attractive for two-dimensional (opto)electronics or as an interlayer for heteroepitaxy [31–35]. The physics of high-temperature chemical vapor deposition (CVD) of h-BN using carbon-free precursors has been studied by Bansal et al. [36].

In its tetrahedrally coordinated sp^3-bonded structure, BN can occur in multiple polymorphs. The wurtzite structure (w-BN) can potentially be alloyed with III-nitrides and grown lattice-matched on GaN template substrates to achieve wider bandgaps, which are useful for charge confinement in high-power electronic devices or quantum barriers in UV–vis optoelectronic devices [37, 38], However, BN is very dissimilar to the III-nitrides in terms of lattice parameters and stable crystalline phase; therefore, random alloys of B-III-N with more than a few percent of boron are difficult to attain [39–42]. In their review, Sarker and Mazumder summarize the developments of B-III-N alloys and provide insights into the microstructures of B-III-N films as demonstrated by local microstructural and atomic-scale chemical analyses [43].

Another sp^3-bonded polymorph of BN is zinc-blende cubic (c-BN). This structure has a very large bandgap energy (~ 6.4 eV) [44], boasts an extremely high thermal conductivity second only to diamond [45], possesses arguably the highest breakdown field in the UWBG family, and can be doped either *n*-type or *p*-type [46–51], thereby making it a strong competitor for future high-power, high-frequency, and high-temperature electronics. To date, however, it has remained difficult to achieve device-quality c-BN using conventional MBE or MOCVD techniques since the cubic structure is metastable under ambient conditions. In general, it is believed that the nucleation of c-BN requires energetic bombardment of the growing surface with charged or neutral ions, regardless of the synthesis approach [52]. A multitude of factors, including degree of ion bombardment, strain, impurity concentration, and growth temperature, is important in determining the quality of the c-BN films [53–57].

Diamond

Recent progress on large wafers and device processing technologies has propelled diamond, which has a bandgap of 5.5 eV, onto the stage of high-power and high-frequency electronics [58]. The figures of merit of diamond devices are extremely high because of high carrier mobility (4500 cm^2/V s for electrons, 3800 cm^2/V s for holes) [59], large breakdown field (> 10 MV/cm), and high thermal conductivity (2200 W/m K) [60].

CVD is widely adopted for the growth of both substrates and epitaxial layers of diamond. Two promising techniques for realizing large wafers at low production cost are the direct wafer method (lift-off) and hetereoepitaxial growth. The former technique involves implanting carbon ions into the subsurface region of a diamond seed crystal to create a defective layer, followed by homoepitaxial growth on the seed crystal by CVD that simultaneously turns the defective layer into graphite. The grown film, a so-called clone-plate, is lifted off by etching the graphitized layer electrochemically [61]. Heteroepitaxial growth of diamond can be performed on Si, 3C-SiC, Pt, and Ir with lattice mismatches of 52%, 22%, 10%, and 7.6%, respectively [58]. Thanks to the small misfit presented by Ir, freestanding diamond wafers larger than 90 mm in diameter [62] and wafers with excellent structural quality [63] have been realized.

High-power capability of diamond devices was first confirmed on Schottky barrier diodes (SBDs) with boron-doped *p*-type layers [64]. The breakdown field of diamond SBDs reaches > 7 MV/cm without edge termination [65]. Diamond SBDs also show low leakage current and short turn-off transient with small reverse recovery time and charges even at elevated temperatures [58]. However, their specific on-resistance is high at room temperature and decreases only when the ambient/junction temperature exceeds 200 °C to increase the activation of the relatively deep boron acceptors (ionization energy ~ 370 meV [66]). To solve this problem, a new structure known as the Schottky *pn*-junction diode (SPND) has been proposed [67].

By precisely controlling the donor concentration in the SPND, holes injected from the impurity band of a p^+ anode drift across a depleted *n*-type layer with high velocity even under forward-bias conditions to realize extremely low on-resistance with high forward current density > 20 kA/cm^2 at room temperature. The SPND is expected to be useful for high-power radio-frequency applications because of its low capacitance, specific on-resistance, and forward voltage drop [68].

For switching devices, high-voltage or high-breakdown-field operation has been reported for metal–semiconductor field-effect transistors (MESFETs) [69], junction FETs (JFETs) [70], and deep-depletion diamond metal–oxide–semiconductor FETs (D3MOSFETs) [71]. Those FET devices use a bulk boron-doped *p*-type layer as the conducting channel, which leads to low current density at room temperature and increasing current density at elevated temperatures, similarly to the SBDs. Current controllability at room temperature can be dramatically enhanced using a two-dimensional hole gas (2DHG) channel [72–74], formed using surface-transfer doping when the diamond surface is terminated by hydrogen [75]. Hydrogen termination lowers the ionization energy of diamond, driving electron transfer from the valence band at the diamond surface into an acceptor layer consisting of molecular adsorbates or a transition metal oxide such as MoO_3 [76]. This gives rise to *p*-type surface conductivity, with holes confined to a thin subsurface layer useful for reducing short-channel effects in high-frequency devices [73]. Output current densities of 2DHG channels reach 1.3 A/mm and 12 kA/cm^2 for lateral [77] and vertical [78] configurations, respectively. Inversion *p*-type channel has also been confirmed on MOSFETs fabricated on phosphorous-doped *n*-type diamond [79], which realizes normally off operation and opens the door for practical applications. Reduction of interface-state density, which can be accomplished by using a 2D material free of dangling bonds as the gate insulator, is key to the improvement of channel mobility and current capability of the devices [80], as shown in Fig. 3. Recently, a hydrogen-terminated diamond FET with high channel mobility of 680 cm^2/V s using a h-BN/diamond heterostructure was reported [81]. It is predicted that a strain-mediated rippled structure developed in the h-BN layer can enhance charge transfer across the h-BN/diamond interface [82].

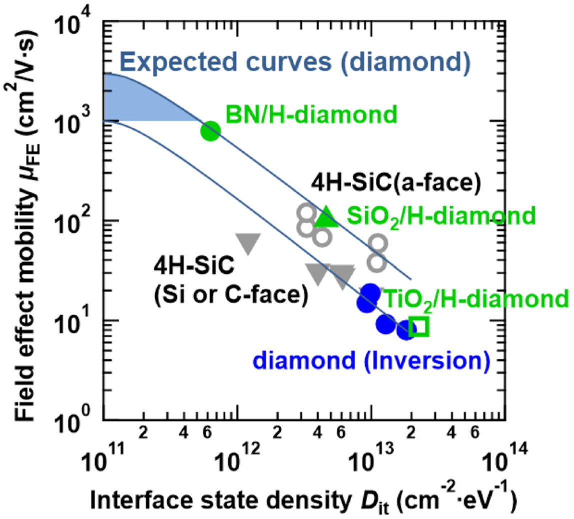

Figure 3: Correlation between field-effect mobility and interface-state density for inversion channel diamond and 4H-SiC MOSFETs. Adapted from [80], with the permission of AIP Publishing.

Oxides

Oxides present a fascinating range of tunable physical properties, including conductivities ranging from insulating through semiconducting to superconducting, magnetism, and piezo-/ferro-/antiferro-electricity. This versatility makes oxides a materials class with high potential for new generations of electronic devices. Applications in power electronics and solar-blind UV detection can particularly benefit from UWBG semiconducting oxides. Compared to the widely explored III-nitrides, these oxides are still in their infancy, except for β-Ga_2O_3 which has been intensely studied over the last decade.

Like the quest to engineer GaN, harnessing oxides for (opto)electronic devices requires high-quality growth of bulk crystals and epitaxial layers with well-defined doping. A broad understanding of device-relevant physical properties is also essential. Bulk oxide crystals provide not only workhorse materials for the extraction of material properties, such as the mobility of electrons as discussed by Galazka et al. [83], but also substrates for homoepitaxy of thin films to achieve the highest structural quality. A versatile tool proven to pioneer novel oxide thin-film systems with highest quality is MBE, as discussed in a review by Nunn et al. [84].

In the following, we briefly review a selection of promising UWBG oxide materials ranging from binary oxides to ternary spinel and complex oxides, whose key materials properties are summarized in Table 1. A common feature of most UWBG oxides is that they can only be doped *n*-type with maximum Hall electron mobilities on the order of 100 to 300 cm^2/V s [83], which limits their application space to unipolar devices unless hetero-*pn*-junctions are used. Often, the bandgaps of oxides were measured by the optical absorption of thin films. As a consequence, only direct transitions with large absorption coefficient or dipole momentum (e.g., from conduction band minimum to a lower-lying valence band at the Gamma point) were identified, resulting in a wider apparent "optical" bandgap than the fundamental indirect or direct but dipole-forbidden bandgap with weak optical absorption. Table 1 lists both types of bandgaps since the optical bandgap is relevant

TABLE 1: Physical properties of selected UWBG oxides. "UID" stands for "unintentionally doped" due to point defects, hydrogen, or unspecified impurities.

Oxide	Crystal structure	Fundamental bandgap (eV)	Optical bandgap (eV)	*n*- or *p*-type (dopant)	Maximum electron mobility (cm^2/V s)	Maximum hole mobility (cm^2/V s)	Thermal conductivity (W/m K)	Articles in this focus issue
β-Ga_2O_3	Monoclinic	4.8[a] [166]	4.4–5.5[b,c] [97–101]	*n* (Si, Ge, Sn)	~200	–	11–29[b] [103, 104]	[83]
SnO_2	Rutile	3.7	–	*n* (Sb)	260	–	55–98[b] [167]	[83]
r-GeO_2	Rutile	4.7 [154]	–	*n* (Sb,As,F)[d] + *p* (Al)[d] [150]	244–377[b,d] [152]	27–29[d] [152]	37–58[b] [151]	–
$ZnGa_2O_4$	Cubic spinel	4.0–4.3 [84]	4.6	*n* (UID)	107		22 [168]	[83, 84]
$MgGa_2O_4$	Inverse spinel	4.9 [84]	–	*n* (UID)	7	–	16 [169]	[83, 84]
$BaSnO_3$	Cubic perovskite	3.0	–	*n* (La) + *p* (K,N)	320 [170]	–	13 [171]	[83, 84]
$SrSnO_3$	Orthorhombic (Pseudo-double cubic perovskite)	4.1 [84]	4.6 [172]	*n* (La)	72	–	–	[84]
$(La_{0.75}Sr_{0.25})CrO_3$ [163]	Perovskite	2.2 [173]	4.6	*p* (Sr)	–	0.03	–	–
Ba_2BiTaO_6 [163]	Double perovskite	–	4.5	*p* (UID)	–	30	–	–
$CuBO_2$ [163]	Delafossite	2.2	4.5	*p* (UID)		100	–	–
$(Ir_{0.4}Ga_{0.6})_2O_3$	Corundum	4.25	–	*p* (UID, Mg)	–	–	–	[165]

[a] There is general consensus that β-Ga_2O_3 has an indirect fundamental bandgap of ~ 4.8 eV and a slightly larger direct bandgap (difference < 0.05 eV).

[b] Anisotropic; the lowest and highest values are given.

[c] Optical absorption edge can be below the fundamental bandgap due to excitonic effects.

[d] Theoretical prediction.

to optoelectronics applications (UV detectors, transparent conductors) and the fundamental bandgap determines the breakdown electric field for power electronics applications.

Binary oxides

β-Ga_2O_3

The most mature, benchmark binary UWBG oxide is β-Ga_2O_3, whose monoclinic β-gallia crystal structure is the most thermodynamically stable polymorph of Ga_2O_3 [85]. This material has attracted significant attention for power electronics applications because of a large 4.8-eV bandgap, controllable *n*-type doping with Si/Sn/Ge, and relatively high electron mobility of ~ 200 cm^2/V s [86–89]. With a critical field strength approximately three times that of SiC and GaN, β-Ga_2O_3 offers greater intrinsic power conversion efficiencies and further expansion of the operating-voltage–switching-frequency power electronics application space. Melt-grown native substrates are available for β-Ga_2O_3, with 4-inch substrates already commercially available, indicating a path to commercially viable Ga_2O_3 devices [90]. Due to its wide bandgap, broadband transparency, low cost, and high thermal/chemical stability, β-Ga_2O_3 has also emerged as a new platform for UV–vis nonlinear optics and integrated photonics such as waveguides and solar-blind photodetectors [91, 92]. Successful development of processing techniques, such as ohmic contacts [93] and etching [94, 95] (Fig. 4), enables complex device structures to be fabricated. The monoclinic lattice of β-Ga_2O_3 leads to pronounced anisotropy in optical, dielectric, and thermal properties [96–104], yet surprisingly maintains near-isotropic electrical conductivity [105]. Lack of *p*-type doping [106–108] and low thermal conductivity [103, 104, 109] pose fundamental limitations to the design of β-Ga_2O_3 devices.

Epitaxial growth techniques developed for β-Ga_2O_3 include MBE [110–112], halide vapor phase epitaxy (HVPE) [113], MOCVD [114], pulsed laser deposition (PLD) [115], and low-pressure chemical vapor deposition (LPCVD) [116]. In the early stages of development, epitaxy of β-Ga_2O_3 was mostly explored by MBE, with typical growth rates of 1–5 nm/min for oxygen-plasma-assisted growths and about 2× higher for ozone-assisted growths. While MBE is suitable for the epitaxy of lateral β-Ga_2O_3 devices, HVPE has been a popular technique for growing vertical devices owing to its capabilities of achieving much higher growth rates (> 10 µm/h) and low background electron densities (< 10^{13} cm^{-3}) [117], which are desirable attributes for obtaining thick, lightly doped drift layers required for high breakdown. As a strong competitor of HVPE, MOCVD has also been adopted for growing homoepitaxial Ga_2O_3 films with smooth morphology, controllable *n*-type doping, and fast growth rates up to about 10 µm/h [118]. High-purity epitaxial films demonstrating superior electronic qualities, including a room-temperature carrier concentration of low 10^{14} cm^{-3} [119], a compensating acceptor concentration as low as 2×10^{13} cm^{-3} (< 0.1% donor

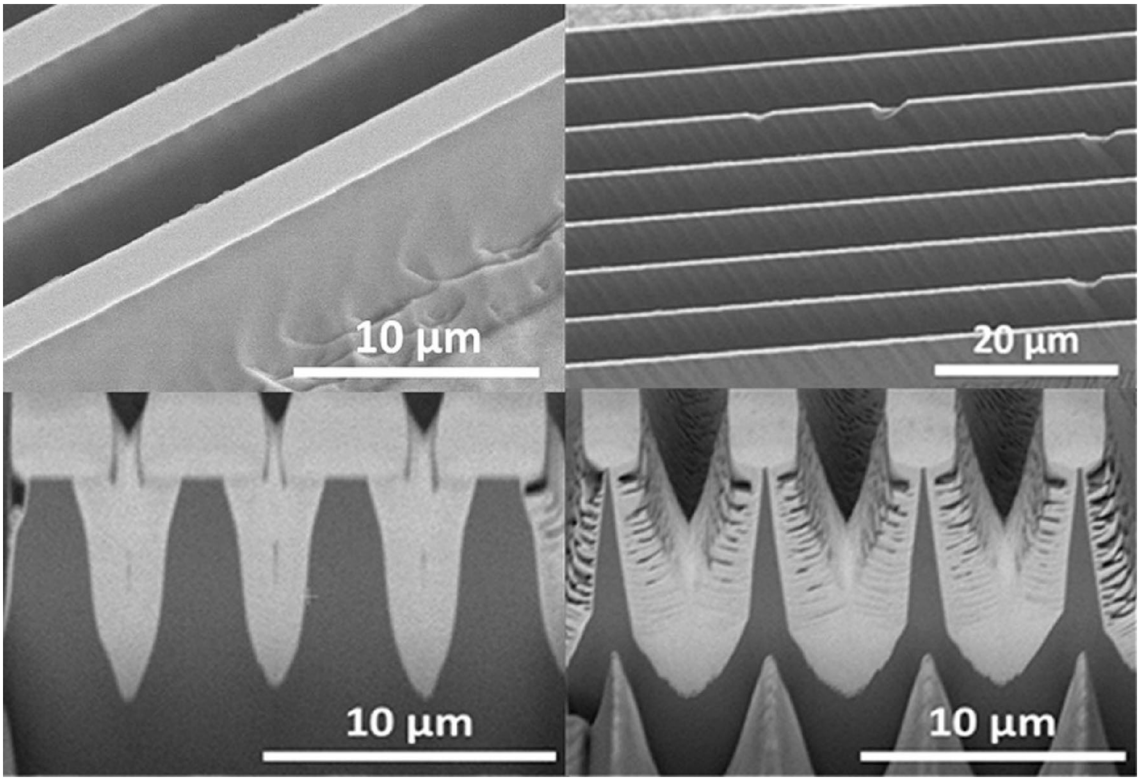

Figure 4: β-Ga_2O_3 fin arrays formed by metal-assisted chemical etching (MacEtch) with high aspect ratio and low-damage sidewall surfaces. Reprinted with permission from [94]. Copyright 2019, American Chemical Society.

compensation) [120], and a low-temperature electron mobility exceeding 10^4 cm^2/V s, have been reported [121].

Alloys between Ga_2O_3 and Al_2O_3 present a rich material space with unique properties that make them attractive candidates as UWBG semiconductors. Modulation-doped field-effect transistors (MODFETs) that utilize β-$(Al_xGa_{1-x})_2O_3$/Ga_2O_3 heterostructures can offer advantages of high sheet-charge density and excellent electron mobility from a 2DEG localized at the heterointerface [122–127]. However, alloying within the $(Al_xGa_{1-x})_2O_3$ system is complicated by the variety of structures and local coordination environments that can be adopted by both parent compounds Ga_2O_3 and Al_2O_3 (Fig. 5) whose ground-state crystal structures are the monoclinic β phase and the corundum α phase, respectively. The Al composition of most epitaxially grown β-$(Al_xGa_{1-x})_2O_3$ has been limited to about 30%, with higher incorporation tending to drive structural degradation, phase segregation, and the formation of γ-phase inclusions [128–132]. The highest Al content of 52% in β-$(Al_xGa_{1-x})_2O_3$ is achieved by MOCVD in (100)-oriented films [133, 134]. The thermodynamics of Al incorporation in Ga_2O_3, and the resulting effects on crystal structure and the optical and electronic properties of $(Al_xGa_{1-x})_2O_3$ alloys, are reviewed by Varley [135].

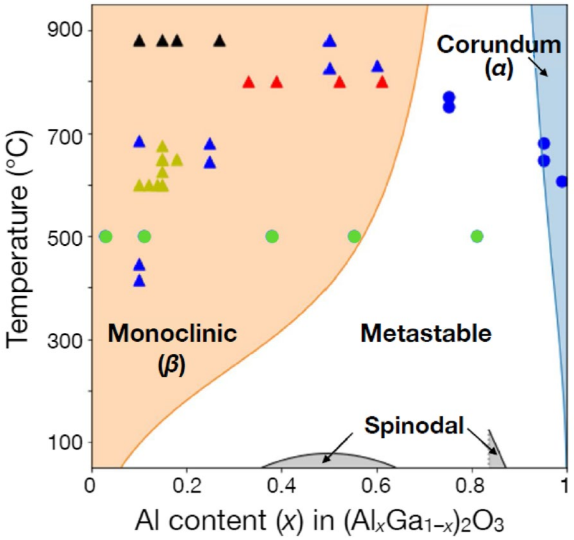

Figure 5: Calculated phase diagram of $(Al_xGa_{1-x})_2O_3$ alloys. Experimental points are included for monoclinic β-$(Al_xGa_{1-x})_2O_3$ (triangles) and corundum α-$(Al_xGa_{1-x})_2O_3$ (circles) grown by different techniques. Reprinted by permission from [135], copyright 2021.

α-Ga_2O_3

Lately, there is increasing interest in the metastable polymorphs of Ga_2O_3, among which α-Ga_2O_3 possesses the largest bandgap of about 5.3 eV [136, 137]. α-Ga_2O_3 can be grown heteroepitaxially with high quality on the c-, m-, a-, or r- planes of isostructural α-Al_2O_3 substrates (sapphire) by mist-CVD [136, 138–140], MBE [141–143], MOCVD [144, 145], or PLD [146, 147], enabling the full compositional range of α-$(Al_xGa_{1-x})_2O_3$ from Ga_2O_3 to Al_2O_3 to be covered without miscibility gaps to allow bandgap engineering for α-Ga_2O_3-based heterostructures from 5.3 to 8.8 eV [138, 142, 145, 147]. Strain relaxation of α-$(Al_xGa_{1-x})_2O_3$ on sapphire is anisotropic and its mechanisms have been investigated [148, 149].

Rutile GeO_2

A series of recent publications predicts rutile GeO_2 (r-GeO_2) to be an UWBG semiconductor that can outperform Ga_2O_3 in terms of device efficiency [150–153]. r-GeO_2 has a bandgap (~ 4.7 eV [150, 154]) similar to that of Ga_2O_3. Its dielectric constant, predicted electron and hole mobilities [152], and thermal conductivity [151] are, however, higher than those of Ga_2O_3, thus bringing beneficial consequences for power-device efficiency. In addition, the predicted prospects for *p*-type conductivity in GeO_2 [150, 155] is extremely attractive as it would enable the realization of r-GeO_2 *pn*-junctions, thereby dramatically widening the device application space to bipolar devices, including *pn*-junction field management for high-voltage devices. Sb and Al are theoretically predicted to be viable donor and acceptor dopants, respectively [150]. The feasibility of bulk growth by solution top-seeding [156] and from the flux [155], as well as of epitaxial growth by MBE [157] (yet at a low growth rate of 10 nm/h) and mist-CVD [158] (at much higher growth rates of up to 1.7 µm/h), has already been experimentally demonstrated. Definitive understandings of doping and charge carrier transport properties are yet to be developed.

Rutile SnO_2

A relatively narrow bandgap of about 3.7 eV does not qualify the classical binary oxide rutile SnO_2 as a true UWBG semiconductor. Nonetheless, this material's combination of significantly higher thermal conductivity and higher electron mobility than most UWBG oxides are appealing for device applications, not to mention the potential for bandgap engineering when alloyed with r-GeO_2.

Ternary oxides

Spinels

The ternary spinel oxides $ZnGa_2O_4$ and $MgGa_2O_4$ provide bandgaps similar to that of β-Ga_2O_3. Their lower electron mobilities [83] and structure-related propensity for antisite defects [84] that carry detrimental implications on the control of carrier concentrations may, however, explain the fact that these oxides are so far only investigated for applications in photodetectors [159] or as phosphors [160, 161] rather than for power electronic devices.

Complex oxides

Ternary complex oxides of general stoichiometry ABO_3 (with cations A and B) provide, based on the choice of A and B as well as strain state, a wealth of (emergent) physical phenomena resulting in a fully tunable spectrum of conductivities as well as magnetic and dielectric properties [84]. At the same time, their common cubic (or pseudocubic orthorhombic) perovskite crystal structure provides the basis for monolithic integration of those properties in epitaxial, multifunctional heterostructures for novel devices. While the prototypical wide-bandgap semiconducting complex oxide $SrTiO_3$ suffers from a low electron mobility (< 10 cm^2/V s) at room temperature, the stannates have been demonstrated to alleviate this issue. To this end, $BaSnO_3$ has recently been demonstrated to exhibit the highest room-temperature electron mobility (> 200 cm^2/V s) among the complex oxides [83, 84], and $SrSnO_3$ has already been made into a demonstrator MESFET device [162] since it offers reasonable electron mobilities in combination with a large bandgap.

p-type oxides

UWBG *p*-type oxides are rare, largely unexplored, and typically suffer from ultra-low hole mobilities (< 1 cm^2/V s). A review by Zhang et al. [163] on *p*-type transparent conducting oxides indicates that *p*-type oxides with optical bandgaps above 4 eV, such as the delafossite $CuBO_2$ (with exceptionally high hole mobility of 100 cm^2/V s) or perovskite Sr-doped $LaCrO_3$ (with low hole mobility of 0.03 cm^2/V s), exhibit fundamental bandgaps (either dipole-forbidden direct or indirect) around 2 eV. A potential exception is the double perovskite oxide Ba_2BiTaO_6 [164] with an optical bandgap > 4.5 eV (fundamental bandgap yet to be experimentally explored) and hole mobility of 30 cm^2/V s, albeit at low achievable hole concentrations on the order of 10^{14} cm^{-3}.

Kaneko and Fujita have demonstrated how alloying a *p*-type oxide α-Ir_2O_3 (bandgap 2.6 eV) with α-Ga_2O_3 results in a true *p*-type UWBG semiconducting α-$(Ir,Ga)_2O_3$ [165].

Summary

This focus issue provides an opportunity for the reader to get a glimpse of the recent advancements in UWBG materials, physics, and related technologies. Despite being in its early years, tremendous progress has been made in this research field in exploiting the fascinating properties of UWBG semiconductors. Fundamental materials-level work in $Al_xGa_{1-x}N$, diamond, β-Ga_2O_3, and other emerging UWBG materials has begun to produce device results commensurate with the fundamental advantages that these materials promise. Open questions remain in UWBG semiconductor research while new ones continuously evolve, to which first-principles computation techniques working in tandem with experimental studies have proven indispensable for improving device performance, discovering new materials with targeted functionalities, and stimulating new research directions [174].

Acknowledgments

Sandia National Laboratories is a multi-mission laboratory managed and operated by National Technology and Engineering Solutions of Sandia, LLC, a wholly owned subsidiary of Honeywell International Inc., for the US Department of Energy's National Nuclear Security Administration under contract DE-NA0003525. This paper describes objective technical results and analysis. Any subjective views or opinions that might be expressed in the paper do not necessarily represent the views of the US Department of Energy or the United States Government.

Data availability

Data sharing not applicable to this article as no datasets were generated or analyzed during the current study.

References

1. J.Y. Tsao, S. Chowdhury, M.A. Hollis, D. Jena, N.M. Johnson, K.A. Jones, R.J. Kaplar, S. Rajan, C.G. Van de Walle, E. Bellotti, C.L. Chua, R. Collazo, M.E. Coltrin, J.A. Cooper, K.R. Evans, S. Graham, T.A. Grotjohn, E.R. Heller, M. Higashiwaki, M.S. Islam, P.W. Juodawlkis, M.A. Khan, A.D. Koehler, J.H. Leach, U.K. Mishra, R.J. Nemanich, R.C.N. Pilawa-Podgurski, J.B. Shealy, Z. Sitar, M.J. Tadjer, A.F. Witulski, M. Wraback, J.A. Simmons, Ultrawide-bandgap semiconductors: research opportunities and challenges. Adv. Electron. Mater. **4**, 1600501 (2018). https://doi.org/10.1002/aelm.201600501
2. O. Slobodyan, J. Flicker, J. Dickerson, J. Shoemaker, A. Binder, T. Smith, S. Goodnick, R. Kaplar, M. Hollis, Analysis of the dependence of critical electric field on semiconductor bandgap. J. Mater. Res. (2021). https://doi.org/10.1557/s43578-021-00465-2
3. A.G. Baca, A.M. Armstrong, A.A. Allerman, E.A. Douglas, C.A. Sanchez, M.P. King, M.E. Coltrin, T.R. Fortune, R.J. Kaplar, An $AlN/Al_{0.85}Ga_{0.15}N$ high electron mobility transistor. Appl. Phys. Lett. **109**, 033509 (2016). https://doi.org/10.1063/1.4959179
4. A.M. Armstrong, B. Klein, A.A. Allerman, E.A. Douglas, A.G. Baca, M.H. Crawford, G.W. Pickrell, C.A. Sanchez, Visible-blind and solar-blind detection induced by defects in AlGaN high electron mobility transistors. J. Appl. Phys. **123**, 114502 (2018). https://doi.org/10.1063/1.4997605
5. P. Pampili, P.J. Parbrook, Doping of III-nitride materials. Mater. Sci. Semi. Proc. **62**, 180 (2017). https://doi.org/10.1016/j.mssp.2016.11.006
6. Y.-H. Liang, E. Towe, Progress in efficient doping of high aluminum-containing group-III nitrides. Appl. Phys. Rev. **5**, 011107 (2018). https://doi.org/10.1063/1.5009349
7. F. Bernardini, V. Fiorentini, D. Vanderbilt, Spontaneous polarization and piezoelectric constants of III-V nitrides. Phys. Rev. B **56**, R10024(R) (1997). https://doi.org/10.1103/PhysRevB.56.R10024
8. D. Jena, S. Heikman, D. Green, D. Buttari, R. Coffie, H. Xing, S. Keller, S. DenBaars, J.S. Speck, U.K. Mishra, Realization of wide electron slabs by polarization bulk doping in graded III-V nitride semiconductor alloys. Appl. Phys. Lett. **81**, 4395 (2002). https://doi.org/10.1063/1.1526161
9. J. Simon, V. Protasenko, C. Lian, H. Xing, D. Jena, Polarization-induced hole doping in wide–band-gap uniaxial semiconductor heterostructures. Science **327**, 60 (2010). https://doi.org/10.1126/science.1183226
10. E. Iliopoulos, T.D. Moustakas, Growth kinetics of AlGaN films by plasma-assisted molecular-beam epitaxy. Appl. Phys. Lett. **81**, 295 (2002). https://doi.org/10.1063/1.1492853
11. H. Tokuda, M. Hatano, N. Yafune, S. Hashimoto, K. Akita, Y. Yamamoto, M. Kuzuhara, High Al composition AlGaN-channel high-electron-mobility transistor on AlN substrate. Appl. Phys. Express **3**, 121003 (2010). https://doi.org/10.1143/APEX.3.121003
12. S.S. Pasayat, N. Hatui, W. Li, C. Gupta, S. Nakamura, S.P. DenBaars, S. Keller, U.K. Mishra, Method of growing elastically relaxed crack-free AlGaN on GaN as substrates for ultra-wide bandgap devices using porous GaN. Appl. Phys. Lett. **117**, 062102 (2020). https://doi.org/10.1063/5.0017948
13. A. Kaminska, K. Koronski, P. Strak, A. Wierzbicka, M. Sobanska, K. Klosek, D.V. Nechaev, V. Pankratov, K. Chernenko, S. Krukowski, Z.R. Zytkiewicz, Defect-related photoluminescence and photoluminescence excitation as a method to study the excitonic bandgap of AlN epitaxial layers: Experimental and *ab*

initio analysis. Appl. Phys. Lett. **117**, 232101 (2020). https://doi.org/10.1063/5.0027743
14. H.M. Foronda, D.A. Hunter, M. Pietsch, L. Sulmoni, A. Muhin, S. Graupeter, N. Susilo, M. Schilling, J. Enslin, K. Irmscher, R.W. Martin, T. Wernicke, M. Kneissl, Electrical properties of (11–22) Si:AlGaN layers at high Al contents by metal-organic vapor phase epitaxy. Appl. Phys. Lett. **117**, 221101 (2020). https://doi.org/10.1063/5.0031468
15. A.M. Armstrong, A.A. Allerman, Evolution of AlGaN deep level defects as a function of alloying and compositional grading and resultant impact on electrical conductivity. Appl. Phys. Lett. **111**, 042103 (2017). https://doi.org/10.1063/1.4996237
16. J.S. Harris, J.N. Baker, B.E. Gaddy, I. Bryan, Z. Bryan, K.J. Mirrielees, P. Reddy, R. Collazo, Z. Sitar, D.L. Irving, On compensation in Si-doped AlN. Appl. Phys. Lett. **112**, 152101 (2018). https://doi.org/10.1063/1.5022794
17. M. Soltani, R. Soref, T. Palacios, D. Englund, AlGaN/AlN integrated photonics platform for the ultraviolet and visible spectral range. Opt. Express **24**, 25415 (2016). https://doi.org/10.1364/OE.24.025415
18. T.P. Chow, R. Tyagi, Wide bandgap compound semiconductors for superior high-voltage unipolar power devices. IEEE Trans. Electron Devices **41**, 1481 (1994). https://doi.org/10.1109/16.297751
19. S. Muhtadi, S.M. Hwang, A. Coleman, F. Asif, G. Simin, M.V.S. Chandrashekhar, A. Khan, High electron mobility transistors with $Al_{0.65}Ga_{0.35}N$ channel layers on thick AlN/sapphire templates. IEEE Electron Device Lett. **38**, 914 (2017). https://doi.org/10.1109/LED.2017.2701651
20. A.A. Allerman, A.M. Armstrong, A.J. Fischer, J.R. Dickerson, M.H. Crawford, M.P. King, M.W. Moseley, J.J. Wierer, R.J. Kaplar, $Al_{0.3}Ga_{0.7}N$ PN diode with breakdown Voltage >1600 V. Electron. Lett. **52**, 1319 (2016). https://doi.org/10.1049/el.2016.1280
21. J. Xie, S. Mia, R. Dalmau, R. Collazo, A. Rice, J. Tweedie, Z. Sitar, Ni/Au Schottky diodes on $Al_xGa_{1-x}N$ ($0.7<x<1$) grown on AlN single crystal substrates. Phys. Status Solidi C **8**, 2407 (2011). https://doi.org/10.1002/pssc.201001009
22. M. Farahmand, C. Garetto, E. Bellotti, K. F. Brennan, M. Goano, E. Ghillino, G. Ghione, J. D. Albrecht, P. P. Ruden, Monte Carlo simulation of electron transport in the III-nitride wurtzite phase materials system: Binaries and ternaries. IEEE Trans. Electron Devices **48**, 535 (2001). https://doi.org/10.1109/16.906448
23. H. Xue, C.H. Lee, K. Hussian, T. Razzak, M. Abdullah, Z. Xia, S.H. Sohel, A. Khan, S. Rajan, W. Lu, $Al_{0.75}Ga_{0.25}N/Al_{0.60}Ga_{0.40}N$ heterojunction field effect transistor with f_T of 40 GHz. Appl. Phys. Express **12**, 066502 (2019). https://doi.org/10.7567/1882-0786/ab1cf9
24. M.E. Coltrin, R.J. Kaplar, Transport and breakdown analysis for improved figure-of-merit for AlGaN power devices. J. Appl. Phys. **121**, 055706 (2017). https://doi.org/10.1063/1.4975346
25. S. Bajaj, F. Akyol, S. Krishnamoorthy, Y. Zhang, S. Rajan, AlGaN channel field effect transistors with graded heterostructure ohmic contacts. Appl. Phys. Lett. **109**, 133508 (2016). https://doi.org/10.1063/1.4963860
26. E.A. Paisley, M. Brumbach, A.A. Allerman, S. Atcitty, A.G. Baca, A.M. Armstrong, R.J. Kaplar, J.F. Ihlefeld, Spectroscopic investigations of band offsets of $MgO|Al_xGa_{1-x}N$ epitaxial heterostructures with varying Al content. Appl. Phys. Lett. **107**, 102101 (2015). https://doi.org/10.1063/1.4930309
27. A. Yoshikawa, R. Hasegawa, T. Morishita, K. Nagase, S. Yamada, J. Grandusky, J. Mann, A. Miller, L.J. Schowalter, Improved efficiency and long lifetime UVC LEDs with wavelengths between 230 and 237 nm. Appl. Phys. Express. **13**, 022001 (2020). https://doi.org/10.35848/1882-0786/ab65fb
28. Z. Zhang, M. Kushimoto, T. Sakai, N. Sugiyama, L.J. Schowalter, C. Sasaoka, H. Amano, A 271.8 nm deep-ultraviolet laser diode for room temperature operation. Appl. Phys. Express **12**, 124003 (2019). https://doi.org/10.7567/1882-0786/ab50e0
29. R. Kirste, B. Sarkar, P. Reddy, Q. Guo, R. Collazo, Z. Sitar, Status of the growth and fabrication of AlGaN-based UV laser diodes for near and mid-UV wavelength. J. Mater. Res. (2021). https://doi.org/10.1557/s43578-021-00443-8
30. C. Cazorla, T. Gould, Polymorphism of bulk boron nitride. Sci. Adv. **5**, eaau5832 (2019). https://doi.org/10.1126/sciadv.aau5832
31. K. Watanabe, T. Taniguchi, H. Kanda, Direct-bandgap properties and evidence for ultraviolet lasing of hexagonal boron nitride single crystal. Nature Mater. **3**, 404 (2004). https://doi.org/10.1038/nmat1134
32. K. Watanabe, T. Taniguchi, T. Niiyama, K. Miya, M. Taniguchi, Far-ultraviolet plane-emission handheld device based on hexagonal boron nitride. Nature Photon. **3**, 591 (2009). https://doi.org/10.1038/nphoton.2009.167
33. R. Bourrellier, S. Meuret, A. Tararan, O. Stéphan, M. Kociak, L.H.G. Tizei, A. Zobelli, Bright UV single photon emission at point defects in h-BN. Nano Lett. **16**, 4317 (2016). https://doi.org/10.1021/acs.nanolett.6b01368
34. T.Q.P. Vuong, G. Cassabois, P. Valvin, E. Rousseau, A. Summerfield, C.J. Mellor, Y. Cho, T.S. Cheng, J.D. Albar, L. Eaves, C.T. Foxon, P.H. Beton, S.V. Novikov, B. Gil, Deep ultraviolet emission in hexagonal boron nitride grown by high-temperature molecular beam epitaxy. 2D Mater. **4**, 021023 (2017). https://doi.org/10.1088/2053-1583/aa604a
35. Y. Kobayashi, K. Kumakura, T. Akasaka, T. Makimoto, Layered boron nitride as a release layer for mechanical transfer of GaN-based devices. Nature **484**, 223 (2012). https://doi.org/10.1038/nature10970
36. A. Bansal, X. Zhang, J.M. Redwing, Gas source chemical vapor deposition of hexagonal boron nitride on C-plane sapphire using B_2H_6 and NH_3. J. Mater. Res. (2021). https://doi.org/10.1557/s43578-021-00446-5

37. L. Williams, E. Kioupakis, BAlGaN alloys nearly lattice-matched to AlN for efficient UV LEDs. Appl. Phys. Lett. **115**, 231103 (2019). https://doi.org/10.1063/1.5129387
38. S. Sakai, Y. Ueta, Y. Terauchi, Band gap energy and band lineup of III–V alloy semiconductors incorporating nitrogen and boron. Jpn. J. Appl. Phys., Part 1 **32**, 4413 (1993). https://doi.org/10.1143/JJAP.32.4413
39. V. Vezin, S. Yatagai, H. Shiraki, S. Uda, Growth of $Ga_{1-x}B_xN$ by molecular beam epitaxy. Jpn. J. Appl. Phys., Part 2 **36**, L1483 (1997). https://doi.org/10.1143/JJAP.36.L1483
40. L. Escalanti, G.L.W. Hart, Boron alloying in GaN. Appl. Phys. Lett. **84**, 705 (2004). https://doi.org/10.1063/1.1644910
41. A. Ougazzaden, S. Gautier, C. Sartel, N. Maloufi, J. Martin, F. Jomard, BGaN materials on GaN/sapphire substrate by MOVPE using N_2 carrier gas. J. Cryst. Growth **289**, 316 (2007). https://doi.org/10.1016/j.jcrysgro.2006.10.072
42. J.-X. Shen, M.E. Turiansky, D. Wickramaratne, C.G. Van de Walle, Thermodynamics of boron incorporation in BGaN. Phys. Rev. Mater. **5**, L030401 (2021). https://doi.org/10.1103/PhysRevMaterials.5.L030401
43. J. Sarker, B. Mazumder, A comprehensive review on the effects of local microstructures and nanoscale chemical features on B-III-nitride films. J. Mater. Res. (2021). https://doi.org/10.1557/s43578-021-00340-0
44. R.M. Chrenko, Ultraviolet and infrared spectra of cubic boron nitride. Solid State Commun. **14**, 511 (1974). https://doi.org/10.1016/0038-1098(74)90978-8
45. K. Chen, B. Song, N.K. Ravichandran, Q. Zheng, X. Chen, H. Lee, H. Sun, S. Li, G.A.G.U. Gamage, F. Tian, Z. Ding, Q. Song, A. Rai, H. Wu, P. Koirala, A.J. Schmidt, K. Watanabe, B. Lv, Z. Ren, L. Shi, D.G. Cahill, T. Taniguchi, D. Broido, G. Chen, Ultrahigh thermal conductivity in isotope-enriched cubic boron nitride. Science **367**, 555 (2020). https://doi.org/10.1126/science.aaz6149
46. T. Taniguchi, T. Teraji, S. Koizumi, K. Watanabe, S. Yamaoka, Appearance of *n*-type semiconducting properties of cBN single crystals grown at high pressure. Jpn. J. Appl. Phys., Part 2 **41**, L109 (2002). https://doi.org/10.1143/JJAP.41.L109
47. C.-X. Wang, G.-W. Yang, T.-C. Zhang, H.-W. Liu, Y.-H. Han, J.-F. Luo, C.-X. Gao, G.-T. Zou, High-quality heterojunction between *p*-type diamond single-crystal film and *n*-type cubic boron nitride bulk single crystal. Appl. Phys. Lett. **83**, 4854 (2003). https://doi.org/10.1063/1.1631059
48. K. Hirama, Y. Taniyasu, H. Yamamoto, K. Kumakura, Control of *n*-type electrical conductivity for cubic boron nitride (c-BN) epitaxial layers by Si doping. Appl. Phys. Lett. **116**, 162104 (2020). https://doi.org/10.1063/1.5143791
49. M.E. Turiansky, D. Wickramaratne, J.L. Lyons, C.G. Van de Walle, Prospects for *n*-type conductivity in cubic boron nitride. Appl. Phys. Lett. **119**, 162105 (2021). https://doi.org/10.1063/5.0069970
50. D. Litvinov, C.A. Taylor II., R. Clarke, Semiconducting cubic boron nitride. Diam. Relat. Mater. **7**, 360 (1998). https://doi.org/10.1016/S0925-9635(97)00216-1
51. T. Taniguchi, S. Koizumi, K. Watanabe, I. Sakaguchi, T. Sekiguchi, S. Yamaoka, High pressure synthesis of UV-light emitting cubic boron nitride single crystals. Diam. Relat. Mater. **12**, 1098 (2003). https://doi.org/10.1016/S0925-9635(02)00330-8
52. K. Hirama, Y. Taniyasu, S. Karimoto, H. Yamamoto, K. Kumakura, Heteroepitaxial growth of single-domain cubic boron nitride films by ion-beam-assisted MBE. Appl. Phys. Express **10**, 035501 (2017). https://doi.org/10.7567/APEX.10.035501
53. T. Yoshida, Vapor phase deposition of cubic boron nitride. Diam. Relat. Mater. **5**, 501 (1996). https://doi.org/10.1016/0925-9635(96)80068-9
54. P.B. Mirkarimi, K.F. McCarty, D.L. Medlin, Review of advances in cubic boron nitride film synthesis. Mater. Sci. Eng. R **21**, 47 (1997). https://doi.org/10.1016/S0927-796X(97)00009-0
55. C.B. Samantaray, R.N. Singh, Review of synthesis and properties of cubic boron nitride (c-BN) thin films. Int. Mater. Rev. **50**, 313 (2005). https://doi.org/10.1179/174328005X67160
56. W.J. Zhang, Y.M. Chong, I. Bello, S.T. Lee, Nucleation, growth and characterization of cubic boron nitride (cBN) films. J. Phys. D: Appl. Phys. **40**, 6159 (2007). https://doi.org/10.1088/0022-3727/40/20/S03
57. X.W. Zhang, Doping and electrical properties of cubic boron nitride thin films: A critical review. Thin Solid Films **544**, 2 (2013). https://doi.org/10.1016/j.tsf.2013.07.001
58. S. Koizumi, H. Umezawa, J. Pernot, M. Suzuki (eds.), *Power Electronics Device Applications of Diamond Semiconductors* (Woodhead Publishing, Duxford, 2018). https://doi.org/10.1016/C2016-0-03999-2
59. J. Isberg, J. Hammersberg, E. Johansson, T. Wikström, D.J. Twitchen, A.J. Whitehead, S.E. Coe, G.A. Scarsbrook, High carrier mobility in single-crystal plasma-deposited diamond. Science **297**, 1670 (2002). https://doi.org/10.1126/science.1074374
60. H. Umezawa, Recent advances in diamond power semiconductor devices. Mater. Sci. Semicond. Process. **78**, 147 (2018). https://doi.org/10.1016/j.mssp.2018.01.007
61. H. Yamada, A. Chayahara, Y. Mokuno, Y. Kato, S. Shikata, A 2-in. mosaic wafer made of a single-crystal diamond. Appl. Phys. Lett. **104**, 102110 (2014). https://doi.org/10.1063/1.4868720
62. M. Schreck, S. Gsell, R. Brescia, M. Fischer, Ion bombardment induced buried lateral growth: the key mechanism for the synthesis of single crystal diamond wafers. Sci. Rep. **7**, 44462 (2017). https://doi.org/10.1038/srep44462
63. S.-W. Kim, R. Takaya, S. Hirano, M. Kasu, Two-inch high-quality (001) diamond heteroepitaxial growth on sapphire

(11$\bar{2}$0) misoriented substrate by step-flow mode. Appl. Phys. Express **14**, 115501 (2021). https://doi.org/10.35848/1882-0786/ac28e7

64. D.J. Twitchen, A.J. Whitehead, S.E. Coe, J. Isberg, J. Hammersberg, T. Wikström, E. Johansson, High-voltage single-crystal diamond diodes. IEEE Trans. Electron Devices **51**, 826 (2004). https://doi.org/10.1109/TED.2004.826867
65. A. Traoré, P. Muret, A. Fiori, D. Eon, E. Gheeraert, J. Pernot, Zr/oxidized diamond interface for high power Schottky diodes. Appl. Phys. Lett. **104**, 052105 (2014). https://doi.org/10.1063/1.4864060
66. K. Thonke, The boron acceptor in diamond. Semicond. Sci. Technol. **18**, S20 (2003). https://doi.org/10.1088/0268-1242/18/3/303
67. T. Makino, S. Tanimoto, Y. Hayashi, H. Kato, N. Tokuda, M. Ogura, D. Takeuchi, K. Oyama, H. Ohashi, H. Okushi, S. Yamasaki, Diamond Schottky-*pn* diode with high forward current density and fast switching operation. Appl. Phys. Lett. **94**, 262101 (2009). https://doi.org/10.1063/1.3159837
68. V. Jha, H. Surdi, M.F. Ahmad, F. Koeck, R.J. Nemanich, S. Goodnick, T.J. Thornton, Diamond Schottky p-i-n diodes for high power RF receiver protectors. Solid-State Electron. **186**, 108154 (2021). https://doi.org/10.1016/j.sse.2021.108154
69. H. Umezawa, T. Matsumoto, S. Shikata, Diamond metal–semiconductor field-effect transistor with breakdown voltage over 1.5 kV. IEEE Electron Device Lett. **35**, 1112 (2014). https://doi.org/10.1109/LED.2014.2356191
70. T. Iwasaki, J. Yaita, H. Kato, T. Makino, M. Ogura, D. Takeuchi, H. Okushi, S. Yamasaki, M. Hatano, 600 V diamond junction field-effect transistors operated at 200 °C. IEEE Electron Device Lett. **35**, 241 (2014). https://doi.org/10.1109/LED.2013.2294969
71. C. Masante, N. Rouger, J. Pernot, Recent progresses in deep-depletion diamond metal–oxide–semiconductor field-effect transistors. J. Phys. D: Appl. Phys. **54**, 233002 (2021). https://doi.org/10.1088/1361-6463/abe8fe
72. H. Kawarada, T. Yamada, D. Xu, H. Tsuboi, Y. Kitabayashi, D. Matsumura, M. Shibata, T. Kudo, M. Inaba, A. Hiraiwa, Durability-enhanced two-dimensional hole gas of C-H diamond surface for complementary power inverter applications. Sci. Rep. **7**, 42368 (2017). https://doi.org/10.1038/srep42368
73. X. Yu, J. Zhou, C. Qi, Z. Cao, Y. Kong, T. Chen, A high frequency hydrogen-terminated diamond MISFET with f_T/f_{max} of 70/80 GHz. IEEE Electron Device Lett. **39**, 1373 (2018). https://doi.org/10.1109/LED.2018.2862158
74. M. Kasu, N.C. Saha, T. Oishi, S.-W. Kim, Fabrication of diamond modulation-doped FETs by NO_2 delta doping in an Al_2O_3 gate layer. Appl. Phys. Express **14**, 051004 (2021). https://doi.org/10.35848/1882-0786/abf445
75. C.I. Pakes, J.A. Garrido, H. Kawarada, Diamond surface conductivity: Properties, devices, and sensors. MRS Bull. **39**, 542 (2014). https://doi.org/10.1557/mrs.2014.95
76. M.R. Neupane, J. Cruz, J.D. Weil, M.N. Groves, Neural network-based study of structural, chemical and electronic properties of doped MoO_3. J. Mater. Res. (2021). https://doi.org/10.1557/s43578-021-00396-y
77. K. Hirama, H. Sato, Y. Harada, H. Yamamoto, M. Kasu, Diamond field-effect transistors with 1.3 A/mm drain current density by Al_2O_3 passivation layer. Jpn. J. Appl. Phys. **51**, 090112 (2012). https://doi.org/10.1143/JJAP.51.090112
78. M. Iwataki, N. Oi, K. Horikawa, S. Amano, J. Nishimura, T. Kageura, M. Inaba, A. Hiraiwa, H. Kawarada, Over 12000 A/cm^2 and 3.2 mΩcm^2 miniaturized vertical-type two-dimensional hole gas diamond MOSFET. IEEE Electron Device Lett. **41**, 111 (2020). https://doi.org/10.1109/LED.2019.2953693
79. X. Zhang, T. Matsumoto, S. Yamasaki, C.E. Nebel, T. Inokuma, N. Tokuda, Inversion-type *p*-channel diamond MOSFET issues. J. Mater. Res. (2021). https://doi.org/10.1557/s43578-021-00317-z
80. T. Matsumoto, H. Kato, T. Makino, M. Ogura, D. Takeuchi, S. Yamasaki, T. Inokuma, N. Tokuda, Inversion channel mobility and interface state density of diamond MOSFET using N-type body with various phosphorus concentrations. Appl. Phys. Lett. **114**, 242101 (2019). https://doi.org/10.1063/1.5100328
81. Y. Sasama, T. Kageura, M. Imura, K. Watanabe, T. Taniguchi, T. Uchihashi, Y. Takahide, High-mobility *p*-channel wide bandgap transistors based on h-BN/diamond heterostructures. arXiv:2102.05982v2 [cond-mat.mtrl-sci] (2021).
82. P.S. Mirabedini, M.R. Neupane, P.A. Greaney, *Ab initio* study of the effect of 2D layer rippling on the electronic properties of 2D/H-terminated diamond (100) heterostructures. J. Mater. Res. (2021). https://doi.org/10.1557/s43578-021-00330-2
83. Z. Galazka, K. Irmscher, M. Pietsch, S. Ganschow, D. Schulz, D. Klimm, I.M. Hanke, T. Schroeder, M. Bickermann, Experimental Hall electron mobility of bulk single crystals of transparent semiconducting oxides. J. Mater. Res. (2021). https://doi.org/10.1557/s43578-021-00353-9
84. W. Nunn, T.K. Truttmann, B. Jalan, A review of molecular-beam epitaxy of wide bandgap complex oxide semiconductors. J. Mater. Res. (2021). https://doi.org/10.1557/s43578-021-00377-1
85. A. Hassa, M. Grundmann, H. von Wenckstern, Progression of group-III sesquioxides: epitaxy, solubility and desorption. J. Phys. D: Appl. Phys. **54**, 223001 (2021). https://doi.org/10.1088/1361-6463/abd4a4
86. M. Higashiwaki, G.H. Jessen, Guest Editorial: The dawn of gallium oxide microelectronics. Appl. Phys. Lett. **112**, 060401 (2018). https://doi.org/10.1063/1.5017845

87. K.D. Chabak, K.D. Leedy, A.J. Green, S. Mou, A.T. Neal, T. Asel, E.R. Heller, N.S. Hendricks, K. Liddy, A. Crespo, N.C. Miller, M.T. Lindquist, N.A. Moser, R.C. Fitch Jr., D.E. Walker Jr., D.L. Dorsey, G.H. Jessen, Lateral β-Ga_2O_3 field effect transistors. Semicond. Sci. Technol. **35**, 013002 (2020). https://doi.org/10.1088/1361-6641/ab55fe
88. M.H. Wong, M. Higashiwaki, Vertical β-Ga_2O_3 power transistors: A review. IEEE Trans. Electron Devices **67**, 3925 (2020). https://doi.org/10.1109/TED.2020.3016609
89. N. Ma, N. Tanen, A. Verma, Z. Guo, T. Luo, H.G. Xing, D. Jena, Intrinsic electron mobility limits in β-Ga_2O_3. Appl. Phys. Lett. **109**, 212101 (2016). https://doi.org/10.1063/1.4968550
90. S.B. Reese, T. Remo, J. Green, A. Zakutayev, How much will gallium oxide power electronics cost? Joule **3**, 903 (2019). https://doi.org/10.1016/j.joule.2019.01.011
91. X. Hou, Y. Zou, M. Ding, Y. Qin, Z. Zhang, X. Ma, P. Tan, S. Yu, X. Zhou, X. Zhao, G. Xu, H. Sun, S. Long, Review of polymorphous Ga_2O_3 materials and their solar-blind photodetector applications. J. Phys. D: Appl. Phys. **54**, 043001 (2021). https://doi.org/10.1088/1361-6463/abbb45
92. J. Zhou, H. Chen, K. Fu, Y. Zhao, Gallium oxide-based optical nonlinear effects and photonics devices. J. Mater. Res. (2021). https://doi.org/10.1557/s43578-021-00397-x
93. M.-H. Lee, R.L. Peterson, Process and characterization of ohmic contacts for beta-phase gallium oxide. J. Mater. Res. (2021). https://doi.org/10.1557/s43578-021-00334-y
94. H.-C. Huang, M. Kim, X. Zhan, K. Chabak, J.D. Kim, A. Kvit, D. Liu, Z. Ma, J.-M. Zuo, X. Li, High aspect ratio β-Ga_2O_3 fin arrays with low-interface charge density by inverse metal-assisted chemical etching. ACS Nano **13**, 8784 (2019). https://doi.org/10.1021/acsnano.9b01709
95. H.-C. Huang, Z. Ren, C. Chan, X. Li, Wet etch, dry etch, and MacEtch of β-Ga_2O_3: A review of characteristics and mechanism. J. Mater. Res. (2021). https://doi.org/10.1557/s43578-021-00413-0
96. N. Ueda, H. Hosono, R. Waseda, H. Kawazoe, Anisotropy of electrical and optical properties in β-Ga_2O_3 single crystals. Appl. Phys. Lett. **71**, 933 (1997). https://doi.org/10.1063/1.119693
97. T. Matsumoto, M. Aoki, A. Kinoshita, T. Aono, Absorption and reflection of vapor grown single crystal platelets of β-Ga_2O_3. Jpn. J. Appl. Phys. **13**, 1578 (1974). https://doi.org/10.1143/JJAP.13.1578
98. C. Sturm, J. Furthmüller, F. Bechstedt, R. Schmidt-Grund, M. Grundmann, Dielectric tensor of monoclinic Ga_2O_3 single crystals in the spectral range 0.5–8.5 eV. APL Mater. **3**, 106106 (2015). https://doi.org/10.1063/1.4934705
99. T. Onuma, S. Saito, K. Sasaki, T. Masui, T. Yamaguchi, T. Honda, M. Higashiwaki, Valence band ordering in β-Ga_2O_3 studied by polarized transmittance and reflectance spectroscopy. Jpn. J. Appl. Phys. **54**, 112601 (2015). https://doi.org/10.7567/JJAP.54.112601
100. F. Ricci, F. Boschi, A. Baraldi, A. Filippetti, M. Higashiwaki, A. Kuramata, V. Fiorentini, R. Fornari, Theoretical and experimental investigation of optical absorption anisotropy in β-Ga_2O_3. J. Phys: Condens. Matter **28**, 224005 (2016). https://doi.org/10.1088/0953-8984/28/22/224005
101. A. Mock, R. Korlacki, C. Briley, V. Darakchieva, B. Monemar, Y. Kumagai, K. Goto, M. Higashiwaki, M. Schubert, Band-to-band transitions, selection rules, effective mass, and excitonic contributions in monoclinic β-Ga_2O_3. Phys. Rev. B **96**, 245205 (2017). https://doi.org/10.1103/PhysRevB.96.245205
102. M. Schubert, R. Korlacki, S. Knight, T. Hofmann, S. Schöche, V. Darakchieva, E. Janzén, B. Monemar, D. Gogova, Q.-T. Thieu, R. Togashi, H. Murakami, Y. Kumagai, K. Goto, A. Kuramata, S. Yamakoshi, M. Higashiwaki, Anisotropy, phonon modes, and free charge carrier parameters in monoclinic β-gallium oxide single crystals. Phys. Rev. B **93**, 125209 (2016). https://doi.org/10.1103/PhysRevB.93.125209
103. Z. Guo, A. Verma, X. Wu, F. Sun, A. Hickman, T. Masui, A. Kuramata, M. Higashiwaki, D. Jena, T. Luo, Anisotropic thermal conductivity in single crystal β-gallium oxide. Appl. Phys. Lett. **106**, 111909 (2015). https://doi.org/10.1063/1.4916078
104. M. Handwerg, R. Mitdank, Z. Galazka, S.F. Fischer, Temperature-dependent thermal conductivity and diffusivity of a Mg-doped insulating β-Ga_2O_3 single crystal along [100], [010] and [001]. Semicond. Sci. Technol. **31**, 125006 (2016). https://doi.org/10.1088/0268-1242/31/12/125006
105. C. Golz, Z. Galazka, J. Lähnemann, V. Hortelano, F. Hatami, W.T. Masselink, O. Bierwagen, Electrical conductivity tensor of β-Ga_2O_3 analyzed by van der Pauw measurements: Inherent anisotropy, off-diagonal element, and the impact of grain boundaries. Phys. Rev. Mater. **3**, 124604 (2019). https://doi.org/10.1103/PhysRevMaterials.3.124604
106. J.B. Varley, A. Janotti, C. Franchini, C.G. Van de Walle, Role of self-trapping in luminescence and *p*-type conductivity of wide-band-gap oxides. Phys. Rev. B **85**, 081109(R) (2012). https://doi.org/10.1103/PhysRevB.85.081109
107. A. Kyrtsos, M. Matsubara, E. Bellotti, On the feasibility of *p*-type Ga_2O_3. Appl. Phys. Lett. **112**, 032108 (2018). https://doi.org/10.1063/1.5009423
108. T. Gake, Y. Kumagai, F. Oba, First-principles study of self-trapped holes and acceptor impurities in Ga_2O_3 polymorphs. Phys. Rev. Mater. **3**, 044603 (2019). https://doi.org/10.1103/PhysRevMaterials.3.044603
109. Y. Song, P. Ranga, Y. Zhang, Z. Feng, H.-L. Huang, M.D. Santia, S.C. Badescu, C.U. Gonzalez-Valle, C. Perez, K. Ferri, R.M. Lavelle, D.W. Snyder, B.A. Klein, J. Deitz, A.G. Baca, J.-P. Maria, B. Ramos-Alvarado, J. Hwang, H. Zhao, X. Wang, S. Krishnamoorthy, B.M. Foley, S. Choi, Thermal conductivity of β-phase

Ga_2O_3 and $(Al_xGa_{1-x})_2O_3$ heteroepitaxial thin films. ACS Appl. Mater. Interfaces **13**, 38477 (2021). https://doi.org/10.1021/acsami.1c08506

110. A. Mauze, J. Speck, Plasma-assisted molecular beam epitaxy 1—Growth, doping, and heterostructures. Chapter 5 in *Gallium Oxide: Material Properties, Crystal Growth, and Devices*. Springer Series in Materials Science, vol. 293, ed. by M. Higashiwaki, S. Fujita (Springer, Cham, 2020). https://doi.org/10.1007/978-3-030-37153-1_5
111. O. Bierwagen, P. Vogt, P. Mazzolini, Plasma-assisted molecular beam epitaxy 2—Fundamentals of suboxide-related growth kinetics, thermodynamics, catalysis, polymorphs, and faceting. Chapter 6 in *Gallium Oxide: Material Properties, Crystal Growth, and Devices*. Springer Series in Materials Science, vol. 293, ed. by M. Higashiwaki, S. Fujita (Springer, Cham, 2020). https://doi.org/10.1007/978-3-030-37153-1_6
112. K. Sasaki, S. Yamakoshi, A. Kuramata, Ozone-enhanced molecular beam epitaxy. Chapter 7 in *Gallium Oxide: Material Properties, Crystal Growth, and Devices*. Springer Series in Materials Science, vol. 293, ed. by M. Higashiwaki, S. Fujita (Springer, Cham, 2020). https://doi.org/10.1007/978-3-030-37153-1_7
113. Y. Kumagai, K. Konishi, K. Goto, H. Murakami, B. Monemar, Halide vapor phase epitaxy 1—Homoepitaxial growth of β-Ga_2O_3 on β-Ga_2O_3 substrates. Chapter 10 in *Gallium Oxide: Material Properties, Crystal Growth, and Devices*. Springer Series in Materials Science, vol. 293, ed. by M. Higashiwaki, S. Fujita (Springer, Cham, 2020). https://doi.org/10.1007/978-3-030-37153-1_10
114. F. Alema, A. Osinsky, Metalorganic chemical vapor deposition 1—Homoepitaxial and heteroepitaxial growth of Ga_2O_3 and related alloys. Chapter 8 in *Gallium Oxide: Material Properties, Crystal Growth, and Devices*. Springer Series in Materials Science, vol. 293, ed. by M. Higashiwaki, S. Fujita (Springer, Cham, 2020). https://doi.org/10.1007/978-3-030-37153-1_8
115. K.D. Leedy, Pulsed laser deposition 1—Homoepitaxial growth of β-Ga_2O_3 on β-Ga_2O_3 substrates. Chapter 14 in *Gallium Oxide: Material Properties, Crystal Growth, and Devices*. Springer Series in Materials Science, vol. 293, ed. by M. Higashiwaki, S. Fujita (Springer, Cham, 2020). https://doi.org/10.1007/978-3-030-37153-1_14
116. H. Zhao, Low-pressure chemical vapor deposition. Chapter 16 in *Gallium Oxide: Material Properties, Crystal Growth, and Devices*. Springer Series in Materials Science, vol. 293, ed. by M. Higashiwaki, S. Fujita (Springer, Cham, 2020). https://doi.org/10.1007/978-3-030-37153-1_16
117. H. Murakami, K. Nomura, K. Goto, K. Sasaki, K. Kawara, Q.T. Thieu, R. Togashi, Y. Kumagai, M. Higashiwaki, A. Kuramata, Homoepitaxial growth of β-Ga_2O_3 layers by halide vapor phase epitaxy. Appl. Phys. Express **8**, 015503 (2015). https://doi.org/10.7567/APEX.8.015503
118. F. Alema, B. Hertog, A. Osinsky, P. Mukhopadhyay, M. Toporkov, W.V. Schoenfeld, Fast growth rate of epitaxial β-Ga_2O_3 by close coupled showerhead MOCVD. J. Cryst. Growth **475**, 77 (2017). https://doi.org/10.1016/j.jcrysgro.2017.06.001
119. F. Alema, Y. Zhang, A. Osinsky, N. Orishchin, N. Valente, A. Mauze, J.S. Speck, Low 10^{14} cm^{-3} free carrier concentration in epitaxial β-Ga_2O_3 grown by MOCVD. APL Mater. **8**, 021110 (2020). https://doi.org/10.1063/1.5132752
120. G. Seryogin, F. Alema, N. Valente, H. Fu, E. Steinbrunner, A.T. Neal, S. Mou, A. Fine, A. Osinsky, MOCVD growth of high purity Ga_2O_3 epitaxial films using trimethylgallium precursor. Appl. Phys. Lett. **117**, 262101 (2020). https://doi.org/10.1063/5.0031484
121. F. Alema, Y. Zhang, A. Osinsky, N. Valente, A. Mauze, T. Itoh, J.S. Speck, Low temperature electron mobility exceeding 10^4 cm^2/Vs in MOCVD grown β-Ga_2O_3. APL Mater. **7**, 121110 (2019). https://doi.org/10.1063/1.5132954
122. A. Kumar, K. Ghosh, U. Singisetti, Low field transport calculation of 2-dimensional electron gas in β-$(Al_xGa_{1-x})_2O_3/Ga_2O_3$ heterostructures. J. Appl. Phys. **128**, 105703 (2020). https://doi.org/10.1063/5.0008578
123. S. Krishnamoorthy, Z. Xia, C. Joishi, Y. Zhang, J. McGlone, J. Johnson, M. Brenner, A.R. Arehart, J. Hwang, S. Lodha, S. Rajan, Modulation-doped β-$(Al_{0.2}Ga_{0.8})_2O_3/Ga_2O_3$ field-effect transistor. Appl. Phys. Lett. **111**, 023502 (2017). https://doi.org/10.1063/1.4993569
124. Y. Zhang, A. Neal, Z. Xia, C. Joishi, J.M. Johnson, Y. Zheng, S. Bajaj, M. Brenner, D. Dorsey, K. Chabak, G. Jessen, J. Hwang, S. Mou, J.P. Heremans, S. Rajan, Demonstration of high mobility and quantum transport in modulation-doped β-$(Al_xGa_{1-x})_2O_3/Ga_2O_3$ heterostructures. Appl. Phys. Lett. **112**, 173502 (2018). https://doi.org/10.1063/1.5025704
125. N.K. Kalarickal, Z. Xia, H.-L. Huang, W. Moore, Y. Liu, M. Brenner, J. Hwang, S. Rajan, β-$(Al_{0.18}Ga_{0.82})_2O_3/Ga_2O_3$ double heterojunction transistor with average field of 5.5 MV/cm. IEEE Electron Device Lett. **42**, 899 (2021). https://doi.org/10.1109/LED.2021.3072052
126. P. Ranga, A. Bhattacharyya, A. Chmielewski, S. Roy, R. Sun, M.A. Scarpulla, N. Alem, S. Krishnamoorthy, Growth and characterization of metalorganic vapor-phase epitaxy-grown β-$(Al_xGa_{1-x})_2O_3/Ga_2O_3$ heterostructure channels. Appl. Phys. Express **14**, 025501 (2021). https://doi.org/10.35848/1882-0786/abd675
127. A. Vaidya, C.N. Saha, U. Singisetti, Enhancement mode β-$(Al_xGa_{1-x})_2O_3/Ga_2O_3$ heterostructure FET (HFET) with high transconductance and cutoff frequency. IEEE Electron Device Lett. **42**, 1444 (2021). https://doi.org/10.1109/LED.2021.3104256
128. A.F.M.A.U. Bhuiyan, Z. Feng, J.M. Johnson, H.-L. Huang, J. Sarker, M. Zhu, M.R. Karim, B. Mazumder, J. Hwang, H. Zhao, Phase transformation in MOCVD growth of

$(Al_xGa_{1-x})_2O_3$ thin films. APL Mater. **8**, 031104 (2020). https://doi.org/10.1063/1.5140345

129. C.S. Chang, N. Tanen, V. Protasenko, T.J. Asel, S. Mou, H.G. Xing, D. Jena, D.A. Muller, γ-phase inclusions as common structural defects in alloyed β-$(Al_xGa_{1-x})_2O_3$ and doped β-Ga_2O_3 films. APL Mater. **9**, 051119 (2021). https://doi.org/10.1063/5.0038861
130. J.M. Johnson, H.-L. Huang, M. Wang, S. Mu, J.B. Varley, A.F.M.A.U. Bhuiyan, Z. Feng, N.K. Kalarickal, S. Rajan, H. Zhao, C.G. Van de Walle, J. Hwang, Atomic scale investigation of aluminum incorporation, defects, and phase stability in β-$(Al_xGa_{1-x})_2O_3$ films. APL. Mater. **9**, 051103 (2021). https://doi.org/10.1063/5.0039769
131. B. Mazumder, J. Sarker, Probing structural and chemical evolution in $(Al_xGa_{1-x})_2O_3$ using atom probe tomography: A review. J. Mater. Res. **36**, 52 (2021). https://doi.org/10.1557/s43578-020-00072-7
132. A.F.M.A.U. Bhuiyan, Z. Feng, L. Meng, H. Zhao, MOCVD growth of (010) β-$(Al_xGa_{1-x})_2O_3$ thin films. J. Mater. Res. (2021). https://doi.org/10.1557/s43578-021-00354-8
133. A.F.M.A.U. Bhuiyan, Z. Feng, J.M. Johnson, H.-L. Huang, J. Hwang, H. Zhao, MOCVD epitaxy of ultrawide bandgap β-$(Al_xGa_{1-x})_2O_3$ with high-Al composition on (100) β-Ga_2O_3 substrates. Cryst. Growth Des. **20**, 6722 (2020). https://doi.org/10.1021/acs.cgd.0c00864
134. A.F.M.A.U. Bhuiyan, Z. Feng, J.M. Johnson, H.-L. Huang, J. Hwang, H. Zhao, Band offsets of (100) β-$(Al_xGa_{1-x})_2O_3/\beta$-$Ga_2O_3$ heterointerfaces grown via MOCVD. Appl. Phys. Lett. **117**, 252105 (2020). https://doi.org/10.1063/5.0031584
135. J. Varley, First-principles calculations of structural, electrical, and optical properties of ultra-wide bandgap $(Al_xGa_{1-x})_2O_3$ alloys. J. Mater. Res. (2021). https://doi.org/10.1557/s43578-021-00371-7
136. D. Shinohara, S. Fujita, Heteroepitaxy of corundum-structured α-Ga_2O_3 thin films on α-Al_2O_3 substrates by ultrasonic mist chemical vapor deposition. Jpn. J. Appl. Phys. **47**, 7311 (2008). https://doi.org/10.1143/JJAP.47.7311
137. H. Peelaers, J.B. Varley, J.S. Speck, C.G. Van de Walle, Structural and electronic properties of Ga_2O_3–Al_2O_3 alloys. Appl. Phys. Lett. **112**, 242101 (2018). https://doi.org/10.1063/1.5036991
138. K. Kaneko, K. Suzuki, Y. Ito, S. Fujita, Growth characteristics of corundum-structured α-$(Al_xGa_{1-x})_2O_3/Ga_2O_3$ heterostructures on sapphire substrates. J. Cryst. Growth **436**, 150 (2016). https://doi.org/10.1016/j.jcrysgro.2015.12.013
139. S. Fujita, M. Oda, K. Kaneko, T. Hitora, Evolution of corundum-structured III-oxide semiconductors: Growth, properties, and devices. Jpn. J. Appl. Phys. **55**, 1202A3 (2016). https://doi.org/10.7567/JJAP.55.1202A3
140. R. Jinno, N. Yoshimura, K. Kaneko, S. Fujita, Enhancement of epitaxial lateral overgrowth in the mist chemical vapor deposition of α-Ga_2O_3 by using a-plane sapphire substrate. Jpn. J. Appl. Phys. **58**, 120912 (2019). https://doi.org/10.7567/1347-4065/ab55c6
141. Z. Cheng, M. Hanke, P. Vogt, O. Bierwagen, A. Trampert, Phase transformation and strain relaxation of Ga_2O_3 on c-plane and a-plane sapphire substrates as studied by synchrotron-based x-ray diffraction. Appl. Phys. Lett. **111**, 162104 (2017). https://doi.org/10.1063/1.4998804
142. R. Jinno, C.S. Chang, T. Onuma, Y. Cho, S.-T. Ho, D. Rowe, M.C. Cao, K. Lee, V. Protasenko, D.G. Schlom, D.A. Muller, H.G. Xing, D. Jena, Crystal orientation dictated epitaxy of ultrawide-bandgap 5.4- to 8.6-eV α-$(AlGa)_2O_3$ on m-plane sapphire. Sci. Adv. **7**, edbd5891 (2021). https://doi.org/10.1126/sciadv.abd5891
143. J.P. McCandless, C.S. Chang, N. Nomoto, J. Casamento, V. Protasenko, P. Vogt, D. Rowe, K. Gann, S.T. Ho, W. Li, R. Jinno, Y. Cho, A.J. Green, K.D. Chabak, D.G. Schlom, M.O. Thompson, D.A. Muller, H.G. Xing, D. Jena, Thermal stability of epitaxial α-Ga_2O_3 and $(Al,Ga)_2O_3$ layers on m-plane sapphire. Appl. Phys. Lett. **119**, 062102 (2021). https://doi.org/10.1063/5.0064278
144. V. Gottschalch, S. Merker, S. Blaurock, M. Kneiß, U. Teschner, M. Grundmann, H. Krautscheid, Heteroepitaxial growth of α-, β-, γ- and κ-Ga_2O_3 phases by metalorganic vapor phase epitaxy. J. Cryst. Growth **510**, 76 (2019). https://doi.org/10.1016/j.jcrysgro.2019.01.018
145. A.F.M.A.U. Bhuiyan, Z. Feng, H.-L. Huang, L. Meng, J. Hwang, H. Zhao, Metalorganic chemical vapor deposition of α-Ga_2O_3 and α-$(Al_xGa_{1-x})_2O_3$ thin films on m-plane sapphire substrates. APL Mater. **9**, 101109 (2021). https://doi.org/10.1063/5.0065087
146. M. Grundmann, T. Stralka, M. Lorenz, Epitaxial growth and strain relaxation of corundum-phase $(Al,Ga)_2O_3$ thin films from pulsed laser deposition at 1000°C on r-plane Al_2O_3. Appl. Phys. Lett. **117**, 242102 (2020). https://doi.org/10.1063/5.0030675
147. A. Hassa, P. Storm, M. Kneiß, D. Splith, H. von Wenckstern, M. Lorenz, M. Grundmann, Structural and elastic properties of α-$(Al_xGa_{1-x})_2O_3$ thin films on (11.0) Al_2O_3 substrates for the entire composition range. Phys. Status Solidi B **258**, 2000394 (2021). https://doi.org/10.1002/pssb.202000394
148. M. Grundmann, M. Lorenz, Anisotropic strain relaxation through prismatic and basal slip in α-$(Al,Ga)_2O_3$ on R-plane Al_2O_3. APL Mater. **8**, 021108 (2020). https://doi.org/10.1063/1.5144744
149. M. Kneiß, D. Splith, H. von Wenckstern, M. Lorenz, T. Schultz, N. Koch, M. Grundmann, Strain states and relaxation for α-$(Al_xGa_{1-x})_2O_3$ thin films on prismatic planes of α-Al_2O_3 in the full composition range: Fundamental difference of a- and m-epitaxial planes in the manifestation of shear strain and lattice tilt. J Mater Res. (2021). https://doi.org/10.1557/s43578-021-00375-3

150. S. Chae, J. Lee, K.A. Mengle, J.T. Heron, E. Kioupakis, Rutile GeO_2: An ultrawide-band-gap semiconductor with ambipolar doping. Appl. Phys. Lett. **114**, 102104 (2019). https://doi.org/10.1063/1.5088370
151. S. Chae, K.A. Mengle, R. Lu, A. Olvera, N. Sanders, J. Lee, P.F.P. Poudeu, J.T. Heron, E. Kioupakis, Thermal conductivity of rutile germanium dioxide. Appl. Phys. Lett. **117**, 102106 (2020). https://doi.org/10.1063/5.0011358
152. K. Bushick, K.A. Mengle, S. Chae, E. Kioupakis, Electron and hole mobility of rutile GeO_2 from first principles: An ultrawide-bandgap semiconductor for power electronics. Appl. Phys. Lett. **117**, 182104 (2020). https://doi.org/10.1063/5.0033284
153. K.A. Mengle, S. Chae, E. Kioupakis, Quasiparticle band structure and optical properties of rutile GeO_2, an ultra-wide-band-gap semiconductor. J. Appl. Phys. **126**, 085703 (2019). https://doi.org/10.1063/1.5111318
154. M. Stapelbroek, B.D. Evans, Exciton structure in the u.v.-absorption edge of tetragonal GeO_2. Solid State Commun. **25**, 959 (1978). https://doi.org/10.1016/0038-1098(78)90311-3
155. C.A. Niedermeier, K. Ide, T. Katase, H. Hosono, T. Kamiya, Shallow valence band of rutile GeO_2 and *p*-type doping. J. Phys. Chem. C **124**, 25721 (2020). https://doi.org/10.1021/acs.jpcc.0c07757
156. J.W. Goodrum, Solution top-seeding: Growth of GeO_2 polymorphs. J. Cryst. Growth **13–14**, 604 (1972). https://doi.org/10.1016/0022-0248(72)90527-1
157. S. Chae, H. Paik, N.M. Vu, E. Kioupakis, J.T. Heron, Epitaxial stabilization of rutile germanium oxide thin film by molecular beam epitaxy. Appl. Phys. Lett. **117**, 072105 (2020). https://doi.org/10.1063/5.0018031
158. H. Takane, K. Kaneko, Establishment of a growth route of crystallized rutile GeO_2 thin film (≥ 1 μm/h) and its structural properties. Appl. Phys. Lett. **119**, 062104 (2021). https://doi.org/10.1063/5.0060785
159. R.-H. Horng, P.-H. Huang, Y.-S. Li, F.-G. Tarntair, C. S. Tan, Reliability study on deep-ultraviolet photodetectors based on $ZnGa_2O_4$ epilayers grown by MOCVD. Appl. Surf. Sci. **555**, 149657 (2021). https://doi.org/10.1016/j.apsusc.2021.149657
160. A. Bessière, S. Jacquart, K. Priolkar, A. Lecointre, B. Viana, D. Gourier, $ZnGa_2O_4$:Cr^{3+}: a new red long-lasting phosphor with high brightness. Opt. Express **19**, 10131 (2011). https://doi.org/10.1364/OE.19.010131
161. N. Basavaraju, S. Sharma, A. Bessière, B. Viana, D. Gourier, K.R. Priolkar, Red persistent luminescence in $MgGa_2O_4$: Cr^{3+}; a new phosphor for *in vivo* imaging. J. Phys. D: Appl. Phys. **46**, 375401 (2013). https://doi.org/10.1088/0022-3727/46/37/375401
162. V.R.S.K. Chaganti, A. Prakash, J. Yue, B. Jalan, S.J. Koester, Demonstration of a depletion-mode $SrSnO_3$ *n*-channel MESFET. IEEE Electron Device Lett. **39**, 1381 (2018). https://doi.org/10.1109/LED.2018.2861320
163. K.H.L. Zhang, K. Xi, M.G. Blamire, R.G. Egdell, *P*-type transparent conducting oxides. J. Phys. **28**, 383002 (2016). https://doi.org/10.1088/0953-8984/28/38/383002
164. A. Bhatia, G. Hautier, T. Nilgianskul, A. Miglio, J. Sun, H.J. Kim, K.H. Kim, S. Chen, G.-M. Rignanese, X. Gonze, J. Suntivich, High-mobility bismuth-based transparent *p*-type oxide from high-throughput material screening. Chem. Mater. **28**, 30 (2016). https://doi.org/10.1021/acs.chemmater.5b03794
165. K. Kaneko, S. Fujita, Novel *p*-type oxides with corundum-structure for gallium oxide electronics. J. Mater. Res. (2021). https://doi.org/10.1557/s43578-021-00439-4
166. H. Peelaers, C.G. Van de Walle, Brillouin zone and band structure of β-Ga_2O_3. Phys. Status Solidi B **252**, 828 (2015). https://doi.org/10.1002/pssb.201451551
167. P. Turkes, C. Pluntke, R. Helbig, Thermal conductivity of SnO_2 single crystals. J. Phys. C: Solid State Phys. **13**, 4941 (1980). https://doi.org/10.1088/0022-3719/13/26/015
168. Z. Galazka, S. Ganschow, R. Schewski, K. Irmscher, D. Klimm, A. Kwasniewski, M. Pietsch, A. Fiedler, I. Schulze-Jonack, M. Albrecht, T. Schröder, M. Bickermann, Ultra-wide bandgap, conductive, high mobility, and high quality melt-grown bulk $ZnGa_2O_4$ single crystals. APL Mater. **7**, 022512 (2019). https://doi.org/10.1063/1.5053867
169. Z. Galazka, *Transparent Semiconducting Oxides: Bulk Crystal Growth and Fundamental Properties* (Jenny Stanford Publishing, New York, 2020). https://doi.org/10.1201/9781003045205
170. H.J. Kim, U. Kim, H.M. Kim, T.H. Kim, H.S. Mun, B.-G. Jeon, K.T. Hong, W.-J. Lee, C. Ju, K.H. Kim, K. Char, High mobility in a stable transparent perovskite oxide. Appl. Phys. Express **5**, 061102 (2012). https://doi.org/10.1143/APEX.5.061102
171. H.J. Kim, T.H. Kim, W.-J. Lee, Y. Chai, J.W. Kim, Y.J. Jwa, S. Chung, S.J. Kim, E. Sohn, S.M. Lee, K.-Y. Choi, K.H. Kim, Determination of temperature-dependent thermal conductivity of a $BaSnO_{3-\delta}$ single crystal by using the 3ω method. Thermochim. Acta **585**, 16 (2014). https://doi.org/10.1016/j.tca.2014.03.036
172. M. Wei, A.V. Sanchela, B. Feng, Y. Ikuhara, H.J. Cho, H. Ohta, High electrical conducting deep-ultraviolet-transparent oxide semiconductor La-doped $SrSnO_3$ exceeding ~3000 S cm^{-1}. Appl. Phys. Lett. **116**, 022103 (2020). https://doi.org/10.1063/1.5128410
173. K.H.L. Zhang, Y. Du, A. Papadogianni, O. Bierwagen, S. Sallis, L.F.J. Piper, M.E. Bowden, V. Shutthanandan, P.V. Sushko, S.A. Chambers, Perovskite Sr-doped $LaCrO_3$ as a new *p*-type transparent conducting oxide. Adv. Mater. **27**, 5191 (2015). https://doi.org/10.1002/adma.201501959
174. E. Kioupakis, S. Chae, K. Bushick, N. Pant, X. Zhang, W. Lee, Theoretical characterization and computational discovery of ultra-wide-band-gap semiconductors with predictive atomistic calculations. J. Mater. Res. (2021). https://doi.org/10.1557/s43578-021-00437-6